Lab on a Chip

A system for the high-throughput measurement of the shear modulus distribution of human red blood cells

Journal:	*Lab on a Chip*
Manuscript ID	LC-ART-03-2020-000283.R1
Article Type:	Paper
Date Submitted by the Author:	25-May-2020
Complete List of Authors:	Saadat, Amir; Stanford University, Chemical Engineering Huyke, Diego; Stanford University, Mechnical Engineering Department Oyarzun, Diego; Stanford University, Mechnical Engineering Department Escobar, Paulina; Pontificia Universidad Católica de Chile Øvreeide, Ingrid; Norwegian University of Science and Technology Shaqfeh, Eric; Stanford University, Chemical Engineering Santiago, Juan; Stanford University, Mechnical Engineering Department

SCHOLARONE™
Manuscripts

A system for the high-throughput measurement of the shear modulus distribution of human red blood cells

Amir Saadat,[1†] Diego A. Huyke,[2†] Diego I. Oyarzun,[2†] Paulina V. Escobar,[4] Ingrid H. Øvreeide,[5] Eric S.G. Shaqfeh,[1,2,3*] and Juan G. Santiago[2*]

[1]Department of Chemical Engineering, [2]Department of Mechanical Engineering, [3]Institute of Computational and Mathematical Engineering Stanford University, Stanford, CA 94305, [4]Department of Mechanical Engineering, Pontificia Universidad Católica de Chile, [5]Department of Physics, Norwegian University of Science and Technology

[†]AS, DAH, and DIO contributed equally to this work

*Corresponding authors: juan.santiago@stanford.edu, esgs@stanford.edu

Abstract

Reduced deformability of red blood cells (RBCs) can affect the hemodynamics of the microcirculation and reduce oxygen transport efficiency. It is also well known that reduced RBC deformability is a signature of various physical disorders, including sepsis, and that the primary determinant of RBC deformability is the membrane shear modulus. To measure the distribution of an individual's RBC shear modulus with high throughput, we a) developed a high-fidelity computational model of RBCs in confined microchannels to inform design decisions; b) created a novel experimental system combining microfluidic flow, imaging, and image analysis; and c) performed automated comparisons between measured quantities and numerical predictions to extract quantitative measures of the RBC shear modulus for each of thousands of cells. We applied our computational simulation platform to construct the appropriate deformability figure(s) of merit to quantify RBC stiffness based on an experimentally measured, steady cell shape in flow through a microchannel. In particular, we determined a shape parameter based on the second moment of the cell shape that is sensitive to the changes in the membrane stiffness and cell size. We then conducted microfluidic experiments and developed custom automated image processing codes to identify and track the position and shape of individual RBCs within micro-constrictions. The fabricated microchannels include a square cross-section imaging region (7 by 7 μm) and we applied order 10 kPa pressure differences to induce order 10 mm s^{-1} cell velocities. The combination of modeling, microfluidics, and imaging enables, for the first time, quantitative measurement of the shear moduli of thousands of RBCs in human blood samples. We demonstrate the high-throughput features by sensitive quantification of the changes in the distribution of RBC stiffness with aging. This combined measurement and computational platform is ultimately intended to diagnose blood cell disorders in patients.

1 Introduction

Deformability is a critical feature of red blood cells (RBCs) and is a particularly important factor in their flow through the microcirculation capillaries or the splenic sinusoids.[1–5] Deformability is affected by many pathological conditions and its alteration can impact the pathophysiology of many diseases.[6,7] Primary reasons for altered deformability are hereditary, mutations, or parasite invasion (e.g., thalassemia,[2] hereditary spherocytosis (HS) and hereditary xerocytosis (HX),[2] and malaria infection[8–10]). However, many secondary biochemical pathways have been shown to influence RBC morphology, biochemistry, and biomechanics and these include RBC hydration,[2] oxidative stress,[11] and myosin activation.[12] As a result, RBC deformability is altered in many blood related diseases such as diabetes,[13,14] sepsis,[15,16] and metabolic syndrome.[17] For example, it was recently discovered that neurodegenerative diseases could be correlated to the deformability of RBCs due to the interrelation between neural activity and blood circulation.[18,19]

Although the RBC structure is quite complex, a few generalizations regarding discoid-shaped RBCs can be made to predict their behavior under deformation. Their membrane is composed of a lipid bilayer as well as a spectrin network and is only a few nanometers thick. This membrane can be approximated as a 2D continuum sheet, defined by three main elastic moduli that describe its resistance to deformation; namely, the area dilatation, shear, and bending modulus.[7,20] However, the membrane warrants treatment as an area inextensible sheet because the area expansion of the membrane has been reported to be negligible.[6] Further, the ratio of bending to shear modulus of RBCs is small, which makes the bending resistance relatively inconsequential.[20,21] The membrane viscosity, meanwhile, provides the major source of energy dissipation.[22,23] This viscosity has shown relatively negligible effects on the stretching behavior of RBCs[24,25] and is further discussed in the Supporting Information (SI), Section S.1. As a result, RBC structure and deformability are largely governed by *the membrane shear modulus*. We note that certain pathological conditions can change the cytoplasmic viscoelasticity and/or bending and area dilatational moduli but these are not considered in our platform. However, we anticipate the application of more comprehensive models as a follow-up to this work. The remainder of this paper is therefore focused on measuring the shear modulus and its distribution over many RBCs in a given individual.

A handful of (low-throughput) experimental approaches have been proposed over the last two decades for the measurement of RBC shear moduli.[7,26,27] Optical tweezers[8,24,28] and micropipette aspiration[29–31] are "standard" approaches. In the optical tweezers technique, a laser beam traps micro-beads adhered to cell surfaces to impose controlled deformations.[24,32] In the micropipette aspiration technique, a pressure difference is used to aspirate a cell inside a micropipette.[29] A high-throughput version of micropipette aspiration can include measurements of hundreds of cells per hour.[33] Ektacytometry,[34] atomic force microscopy (AFM),[35–37] dynamic phase microscopy (DPM),[25] and RBC filterability,[15] have also been proposed to measure the deformability, but all suffer from relatively low throughput.

Typically, high-throughput techniques for the measurement of red blood cell mechanical properties are based on a microfluidic platform that deform and image cells under shear stress. Experimental images are used in conjunction with a constitutive cell model to estimate RBC properties; e.g. deformation,[38–40] Young's modulus,[41] and cytoplasmic viscosity.[41] Examples of high-throughput microfluidic platforms include those developed by Otto el al., who visualized and analyzed RBCs before and after a chemical treatment. However, this work was limited to detection of changes in cell deformation, and no mechanical properties were reported. Reichel et al.[42] found that certain RBC confinements and velocities induce non-unique shapes (e.g. tumbling, tank-treading, parachute, etc.). Thus, their work can provide qualitative information of cell shape but cannot quantify cell mechanical properties. Fregin et al.[41] combined experimental images of cells under shear stress with a Kelvin-Voigt model, but their device can only measure an overall Young's modulus and the cytoplasmic viscosity of RBCs.

Different simulation techniques have been used to quantify the mechanical properties of RBCs.[20,28,40,42–46] For instance, coarse-grained molecular dynamics (CGMD) have been used to include molecular level details in interpreting optical tweezer results and converting those to a membrane shear modulus.[20] However, this method is computationally prohibitive and is not suitable for large-scale simulations of many cells. Dissipative particle dynamics (DPD) is another widely used, particle-based approach to simulate optical tweezers and RBCs in a microchannel.[28,42] This method provides good scalability compared to CGMD but does not solve the Navier-Stokes equations rigorously. The immersed boundary (IB) algorithm is a continuum-level approach which solves the evolution of a moving deformable membrane overlayed on a static Eulerian domain.[47–50] Nevertheless, to the best of our knowledge, CGMD, DPD, and IB have not been used to interpret the results of high-throughput experiments. On the other hand, a considerable fraction of RBC biomechanical models overly simplify the problem, either by assuming a static state for the cell and solving the equilibrium shape under a given hydrodynamic load,[40] using analytical approximate solutions to the Navier-Stokes equation,[51] or neglecting the fluid-membrane interactions.[45,46] These simplifications restrict detailed investigation of the three-dimensional shape of the red blood cells as they flow through non-trivial geometries.

In summary, state-of-the-art methods to measure the shear modulus of RBCs are not high-throughput, and microfluidic platforms for high-throughput measurements of RBC mechanical properties have not yet enabled measurement of the shear modulus. These limitations challenge the development of diagnostic devices based on RBC shear modulus biomarkers. We demonstrate a microfluidic platform, coupled with IB simulations, to address this significant gap in technology. Specifically, our simulation technique is an IB variant which uses a finite-volume method for solving the momentum conservation equations in the domain and a finite-element method for calculating the tension in the membrane.[49] This technique allows evolution of the shape in any complicated non-periodic geometry (such as the one that we use for understanding the cellular motion in the entrance region) and includes the membrane characteristic viscoelastic

properties, such as the membrane elastic moduli as well as cytoplasmic viscosity. In contrast with existing technologies, this approach allows us to measure the shear modulus of individual RBCs and generate shear modulus distributions (for a given individual or multiple individuals) including measurements of up to 75 cells per second of experimental data acquisition.

We note the novelty of our system is the integration of full 3D numerical simulation, high-resolution microfluidic experiments, and automatic image analysis to determine a critical mechanical property of red blood cells with high throughput. The goal of this work is to facilitate and help standardize cell biomechanical measurements. This is important, as a large body of publications on cellular pathology report cell deformability. In this work, we quantify the (wide) distribution of the cell properties within a single sample and show significant variations among samples. We also demonstrate quantitatively and with high statistical certainty changes to RBC properties subject to five weeks of storage.

2 Results and Discussion

2.1 Microfluidic device and high-fidelity simulations: System design

This section provides an overview of the simulation methods and how these were used to guide design of the experimental setup. We implemented an IB numerical model[49] to simulate RBC deformations near the entrance and in periodic channel domains (Fig. 1A). The entrance domain consisted of a single channel with fixed height and tapering-width whereas the periodic channel domain consisted of a single channel constriction with fixed width and height. The relation between the project area of the cell A and the hydraulic diameter of the constriction H was given by the nondimensional confinement parameter ϵ as

$$\epsilon = 2\sqrt{A/\pi}\,/H. \qquad (1)$$

The simulations revealed that, for cell velocities between 2 and 10 mm s^{-1}, RBCs assumed a parachute shape when [confinement] ϵ was greater than about 0.9. Note that if confinement is insufficient (i.e. lower values of ϵ), cell motion can transition from parachute formation to a tumbling motion. This critical value of ϵ depends on the cell velocity as well as the membrane and cytoplasm mechanical properties.[42,52] We chose a 7 by 7 μm cross-section for our channels to increase the likelihood of parachute formation without excessive cell extension due to squeezing (cf. Section 2.2). The latter can introduce large stress on the membrane and negatively impact our shear modulus measurements.[45] A second set of considerations was due to constraints imposed by the imaging system. For example, for equal values of applied pressure, smaller channels offer greater confinement but may also yield velocities which cause blurring of cell images given the time scale of our pulsed light source. The SI, Section S.1, further discusses the development of the numerical model in detail.

In conjunction with our high-fidelity simulations, we performed high-throughput experimental visualizations of RBCs under shear stress. The experimental setup consisted of a custom poly-dimethylsiloxane (PDMS) and glass microfluidic chip, as well as flow control and image acquisition instruments (Fig. 1B and SI, Section S.4). Briefly, the microfluidic chip was visualized on an inverted microscope interfaced with a high-power LED, a scientific-grade complementary metal oxide semiconductor (sCMOS) camera, and associated optical train components. Elastically scattered light from the microfluidic chip was collected using a 20×/0.95 numerical aperture objective. Importantly, camera integration and LED illumination were synchronized to enable effective exposure times as low as 40 µs. The flow control consisted of pressure lines to apply order 10 kPa gauge pressures at the chip inlet reservoir (shown on the left of Fig. 1A). The experimental setup was used to flow and obtain images of RBCs as they traveled through a 7 by 7 µm constriction at velocities of 2-10 mm s^{-1}.

Fig. 1C shows a comparison of RBC images obtained from simulations (top row) and experiments (bottom row). Importantly, both pairs of images contain cells with similar starting positions along the spanwise plane. We note the qualitative agreement between simulated and experimentally imaged RBCs for different entrance conditions.
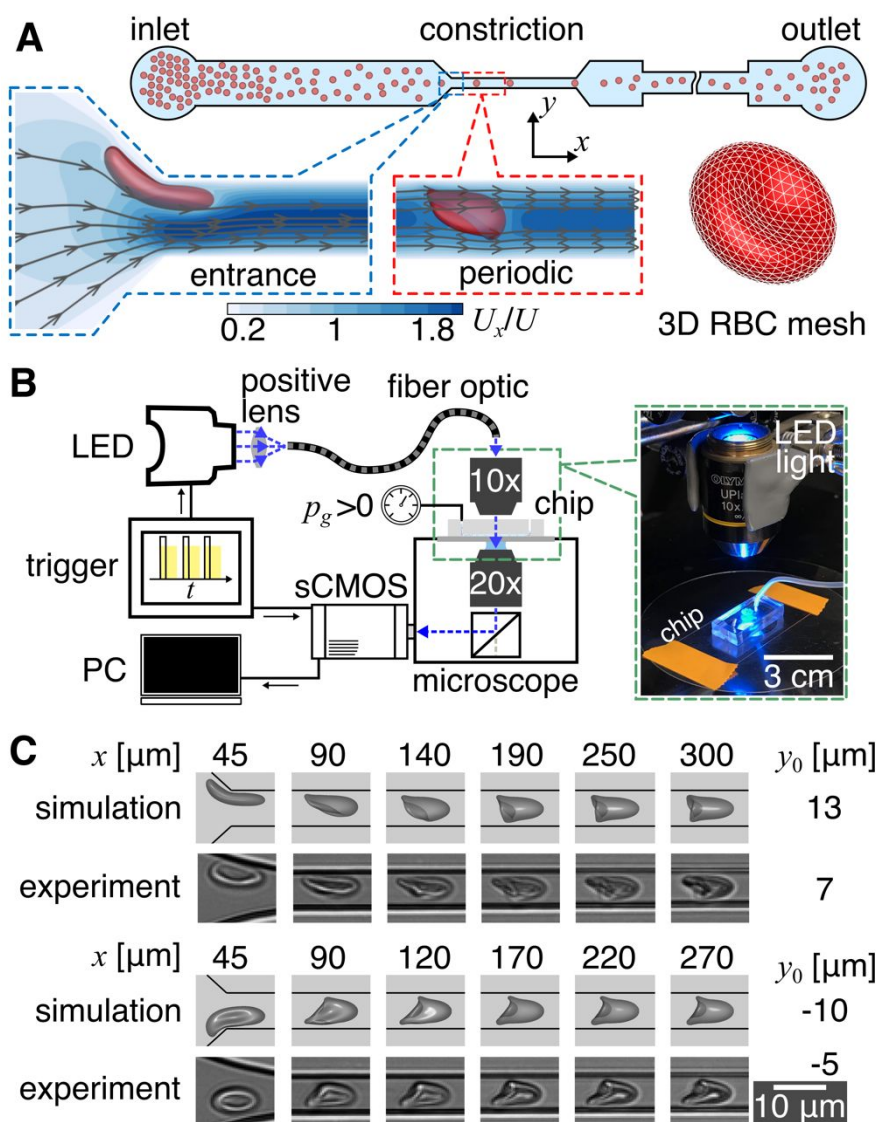
Fig. 1 Overview of high-fidelity numerical simulations and experimental setup. (A) Schematic of the microfluidic chip design (top row) and numerical simulation entrance and periodic domains with example RBC and overlaid velocity magnitude fields (bottom row). Also shown is an example mesh distribution for an individual RBC. (B) Schematic of the experimental fluid flow and cell visualization setup. Camera integration and LED illumination were synchronized to enable image exposures as short as 40 μs. The inset shows an image of the microfluidic chip under bright field illumination. (C) Qualitative comparison of simulation and experimental images of RBCs as they deform and approach a steady-state shape in a constriction with 7 by 7 μm.

2.2 Shear modulus effect on RBC deformation

While the simulations informed experimental conditions, analytical arguments were also used to relate experimental images to simulation results. We discuss the major nondimensional parameters of the system and use these to introduce an RBC shape parameter which is highly sensitive to the shear modulus. In our platform, we hypothesize cell deformation is governed by the capillary number Ca, which is given by

$$Ca = \frac{\eta U}{\mu_s},$$ (2)

where η is the viscosity of the medium (in our experiments we used PBS), U is the bulk fluid velocity inside the constriction, and μ_s is the RBC shear modulus. We note that, in each experiment, η and U are nearly constant and μ_s varies from cell to cell. Other nondimensional parameters, such as a Reynolds number Re, and the RBC cytoplasmic viscosity ratio λ, are discussed in Section 4.1. The challenge is to estimate Ca for every cell in an experiment which is limited to optical detection methods.

After a comparison of varied morphological parameters (e.g, among others, circularity and circular harmonics, described in section 4.2 and SI, section S.2), we found that combinations of Taylor deformation Ta and confinement ϵ provide a one-to-one correspondence to the cell-specific capillary number Ca_{cell}. Also, quantification of Ta based on area moments is less sensitive to image noise than measurements of cell image boundary lengths. Ta (Fig. 2A) is given by

$$Ta = \frac{a - b}{a + b},$$ (3)

where a and b are the major and minor axes of an equivalent ellipse that is obtained based on the second-order moment of the cell image projected onto the plane of view, i.e., xy-plane (cf. SI, Section S.1). Importantly, we note that RBC second-order moments are less sensitive to experimental image noise than the area, major axis length, eccentricity, and perimeter (Fig. S14).

We note that RBCs demonstrate a diverse range of dynamic shape evolution, i.e., including tumbling, tank-threading, as well as symmetric or asymmetric "parachutes" (or "umbrellas")[42,53] especially if the range of ϵ and Ca are not carefully chosen. We therefore chose ϵ (between 0.8 and 1.3) and Ca (between 0.2 and 1.6) to *guarantee a static parachute shape*. This parameter range is comparable to that which occurs physiologically in microcirculation.[54,55] In contrast, for $\epsilon < 0.4$ and $Ca > 0.2$, we observe parachute shapes but also unsteady wobbling dynamics.

Under the specified parameter space, Ta approached a distinct set of steady state values downstream in the channel flow, even for 25% difference in Ca (Fig. 2B) or confinement ϵ (Fig. 2C). We further investigated the impact of the initial condition on the final Ta steady state values using the simulations in the entrance and periodic domains. To this end, we varied the initial

location in y and z directions (offset with respect to the center axis) in Fig. 2D and the orientation angle (rotation with respect to x and y axes) in Fig. 2E. The results highlighted the importance of the initial condition in the transient behavior but note that all trajectories approached the same values of Ta downstream of $x = 300$ μm. The simulations also revealed that for very large values of ϵ (corresponding to larger physiological size of the cells, shown in the inset of Fig. 2F), RBCs are excessively extended and show less sensitivity to variations in shear moduli.
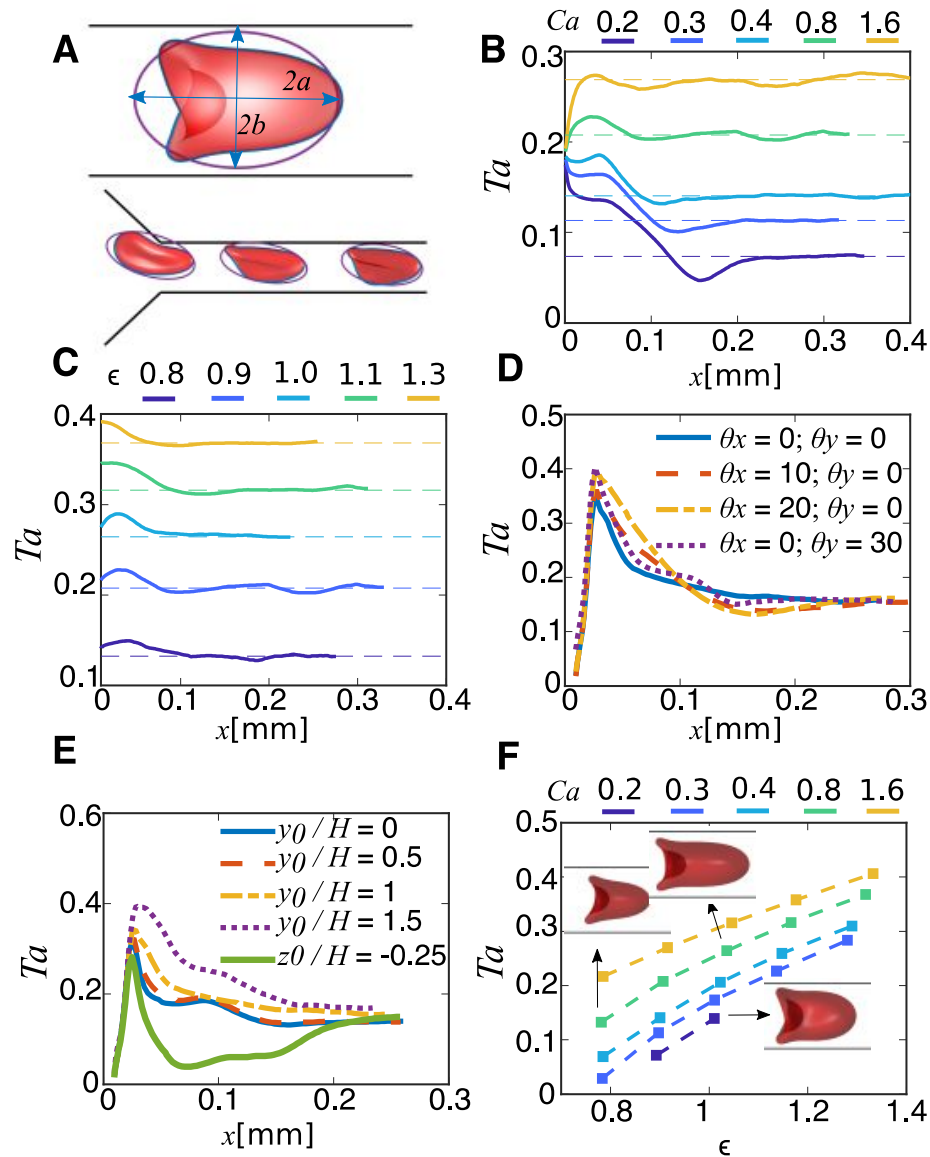

Fig. 2 (A) Equivalent ellipse and the corresponding Taylor deformation Ta for a cell with capillary number $Ca = 0.8$ and confinement $\epsilon = 0.9$. Note that ϵ is varied by changing the surface-to-volume ratio in the range of $1.04 - 1.66$. The major and minor axes are denoted by a and b, respectively. The bottom row shows the cell shapes and their corresponding equivalent

ellipse in the entrance region. (B) The transient evolution of Ta as a function of location along x-axis for different Ca. (C) The transient evolution of Ta vs x for five different confinements. (D)-(E) The transient evolution of Ta as a function of x for several initial RBC orientations and locations with respect to x, y, and z axes. (F) The steady-state values of Ta vs confinement for several Ca. Cell shapes at the steady-state are shown for three conditions.

As will be shown in the next section, the values of Ta and ϵ can be determined experimentally for every individual cell that is tracked in the microfluidic channels. The predictions of Fig. 2F provide the means by which a unique Ca can be identified for specified combinations of Ta and ϵ. However, using this relation to quantify the shear modulus of the measured RBCs would then require knowledge of the ratio of cell velocity U_{cell} to the bulk velocity (i.e. U_{cell}/U, Fig. 3A). We therefore developed a method to extract shear moduli without direct knowledge of bulk velocity. To this end, we computed the unique values of the ratio U_{cell}/U for each combination of Ta and ϵ. The two simulations (Figs. 2F and 3A) therefore enable us to generate a new three-dimensional relation among Ca_{cell}, Ta, and ϵ, where

$$Ca_{cell} = \frac{U_{cell}\eta}{\mu_s}. \tag{4}$$

The value of Ca_{cell} can be then determined for each cell by measuring its Ta and ϵ (Fig. 3B). We then use the measurement of the cell velocity U_{cell} and the continuous-phase viscosity η to determine the RBC shear modulus as $\mu_s = U_{cell}\eta/Ca_{cell}$. Hence, an estimate for the bulk velocity is no longer needed.
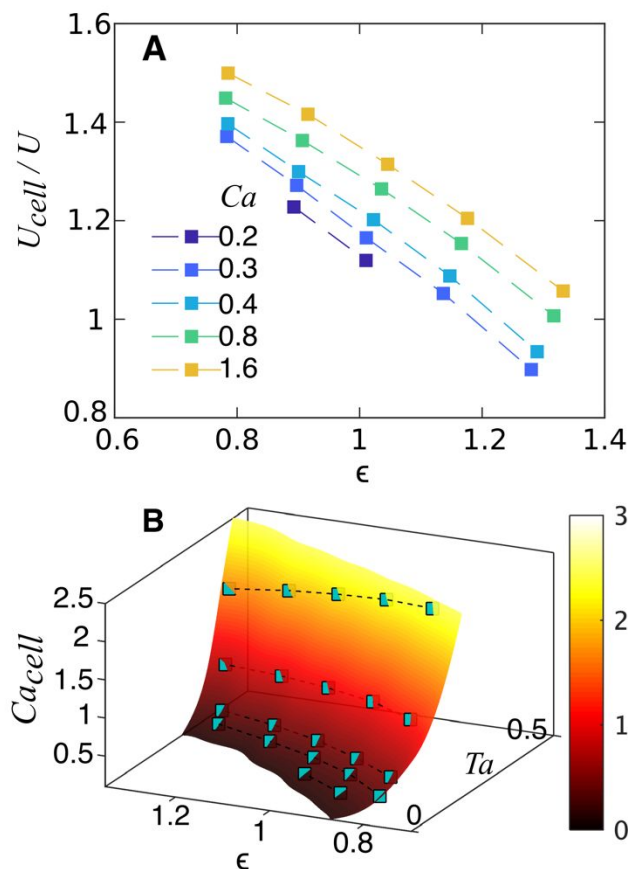
Fig. 3 (A) The steady-state values of the ratio of cell velocity to the bulk velocity U_{cell}/U versus the confinement ϵ for capillary numbers Ca ranging from 0.2 to 1.6. (B) Three-dimensional surface plot of a cell-based capillary number Ca_{cell} as a function of the Taylor deformation Ta and ϵ constructed based on the results shown in Fig. 2F and 3A. The surface color indicates the values of Ca_{cell}. The green symbols are the simulation results. This surface plot permits the extraction of an individual RBC shear modulus given only measurements of its ϵ and Ta as well as U_{cell} and the viscosity of the medium.

Note this alternate capillary number approach is powerful because cell velocity can be measured highly accurately using cell image tracking. By comparison, the bulk velocity in the channel is much more difficult to measure accurately. Consider that bulk velocity depends on the estimate of applied pressure and the hydraulic resistance of the channel. The latter varies dynamically as cells enter and leave the channel and is very sensitivity to uncertainties in the height and width of the channel. Particle imaging velocimetry techniques (such as micro-PIV)[56] would be very difficult due to the depth-of-field of our setup and illumination method. Further, tracer particles are typically dissolved in solution with a nonionic surfactant (e.g. Triton X-100) to prevent wall adhesion, but this surfactant would also lyse RBCs.

2.3 High-throughput tracking and measuring of RBCs

As discussed in section 2.2, estimated measures of the Taylor deformation Ta and confinement ϵ are required to experimentally quantify shear modulus of individual RBCs. Consequently, we deformed cells in flow and imaged up to 75 cells per second as they traveled through 7 by 7 μm constrictions (length of 1 mm) at velocities between 2 and 10 mm s^{-1}. As shown in Fig. 1B, the experimental setup consisted of a custom poly-dimethylsiloxane (PDMS) and glass microfluidic chip, as well as flow control and image acquisition instruments. Experimental images were analyzed in MATLAB (2019a, Mathworks, USA) after performing a moving time-median background subtraction. Briefly, our code used a threshold and centroid computation algorithm to identify all cells in each frame. Cells were tracked from frame to frame using a Chi-square minimization in terms of cell centroid locations to establish the most likely match of each cell in the subsequent frame. Cell centroid locations and cell velocities were determined using morphological image processing and cell image tracking using a Chi-square minimization technique (c.f. Fig. S10). We note that experimental measurements of the fluid bulk velocity (for a flow rate on the order of 10 nL min^{-1}) are difficult, but a cell-based capillary number Ca_{cell} obviates the need for such a measurement. The SI, Section S.3 further describes our experimental setup and image analyses.

Fig. 4A (top) shows the instantaneous RBC velocity in the ordinate and length along the microchannel constriction in the abscissa. Each gray line in the plot corresponds to the trajectory of an individual RBC. The squares correspond to the mean RBC instantaneous velocity; and the uncertainty bars indicate plus and minus one standard deviation. Just upstream of the entrance (at an axial position $x = 0$ μm) the cell velocity is about 1 mm s^{-1}. The cell velocity then rapidly increases as cells enter the channel and reach a near-constant value downstream of at about $x = 150$ μm. The histogram represents the time-average velocity distribution for the steady-state region, downstream of $x = 300$ μm (red box in Fig. 4A). The middle plot of Fig. 4A shows RBC confinement as a function of x, and a confinement ϵ histogram of in the steady-state region. The changes in ϵ are attributed to the underlying distribution of the projected areas of individual RBCs. Finally, the bottom plot of Fig. 4A shows RBC Taylor deformation Ta as a function of x, and a Ta histogram in the steady-state region.

The top plot of Fig. 4B shows the distribution of confinement ϵ for RBCs withdrawn two hours before experiments and RBCs that have been stored in a 4°C fridge for 5 weeks . The mean confinement of fresh and stored RBCs, respectively, is 1.04 and 0.97, while the standard deviation of confinement of fresh and stored RBCs, respectively, is 0.065 and 0.081. This corresponds to a difference in the means of 7%. A higher confinement corresponds to a cell with a larger projected area. The bottom two rows of Fig. 4B show the confinement for separate donors (fresh RBCs) and these exhibit minor differences in confinement.

The top plot of Fig. 4C shows the distribution of Taylor deformation Ta for fresh and 5-weeks stored cells. The mean Taylor deformation of fresh and stored RBCs, respectively, is 0.32 and 0.14, while the standard deviation of Taylor deformation of fresh and stored RBCS,

respectively, is 0.065 and 0.064. This corresponds to a difference in the means of 56%. The dramatically smaller Taylor deformation of the stored RBCs is expected as aging of these cells is known to lead to stiffening.[45] Consequently, the projected area of these aged RBCs, as captured in the experimental images is more circular. The bottom two rows of Fig. 4C show the distribution of Taylor deformation for fresh RBCs and shows very little difference in the mean or standard deviation of Ta.
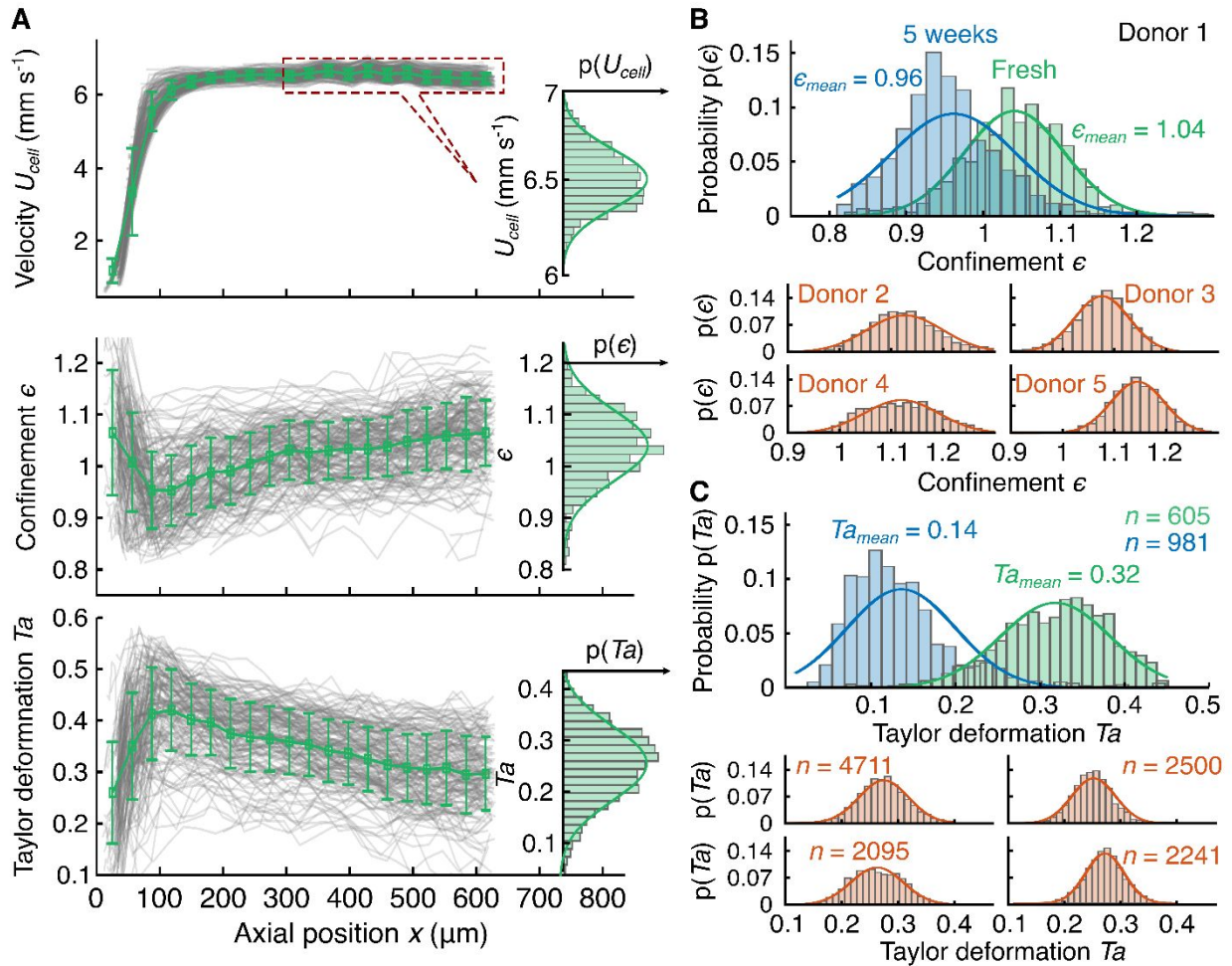

Fig. 4. (A) Experimental transient behavior of cell velocity U_{cell}, confinement ϵ, and Taylor deformation Ta in the entrance region as a function the axial position x. The steady-state probability distribution, namely, p(U_{cell}), p(ϵ), and p(Ta) are shown on the right-hand-side of the transient curves. In the top rows of (B) and (C), p(ϵ) and p(Ta) are respectively shown for Donor 1 RBCs withdrawn two hours before experiments (green) and RBCs that have been stored in a 4°C fridge 5 weeks (blue). The values ϵ_{mean} and Ta_{mean} are, respectively, the mean confinement and Taylor deformation of each group. The middle and bottom rows of (B) and (C) respectively show p(ϵ) and p(Ta) for fresh cells from Donors 2-5. n is the number of cells analyzed in each group.

2.4 Probability density function for shear modulus

We next make a measurement of the shear modulus of individual RBCs by combining high-fidelity simulations and experimental images. To this end, our automatic image processing script analyzes the steady-state shape of a cell (for $x > 300$ um) and measures its confinement ϵ, Taylor deformation Ta, and velocity U_{cell}. Each individual cell was imaged, and its morphological and velocity properties were measured (typically) 20 times, before an average of these was taken. Simulations showed that the steady state confinement and Taylor deformation of any cell corresponds to a cell-specific capillary number Ca_{cell} (Fig. 3B). This relation can be visualized by a projection in the Ta versus ϵ plane (the surface plot in Fig. 5A). Hence, referring to the definition of Ca_{cell} and given U_{cell} (also measured), the shear modulus of the cell was calculated. Fig. 5A additionally shows experimentally measured Ta versus ϵ for fresh ($n = 605$) and cells stored for 5 weeks ($n = 981$) from the same donor. The fresh RBCs generally have a greater Ta and ϵ.

Fig. 5B shows the shear modulus distribution for the same group of cells as Fig. 5A. The shear modulus distribution shows a near lognormal distribution, and so this distribution has been overlaid. It has been shown that the geometric mean is the proper statistical parameter for a log-normal distribution,[57,58] hence, we use this in our analysis below where the mean is denoted with an asterisk to distinguish from an arithmetic mean used for Ta and ϵ (SI, Section S.6). For donor 1, the fresh blood distribution shows a mean shear modulus value 4.2 µN m^{-1}. After 5 weeks of storage, the mean shear modulus increased to 30 µN m^{-1}. The spread of the distribution for the stored RBCs increased from 6.82 to 41 µN m^{-1}. The observed and substantial increase in RBC shear moduli due to storage is consistent with observations reported using optical tweezers.[24,32] This demonstrates our system has sufficient sensitivity (and resolution) to alterations in RBC stiffness.

Fig. 5C shows the shear modulus distribution for four different donors. We found that the distribution for each donor follows a lognormal distribution. The mean shear moduli across Donors 2-5 (not labeled) ranged from 12 to 20 µN m^{-1}. The results suggest that there are donor-to-donor differences in mean shear moduli as large as 16 µN m^{-1} (when compared to fresh Donor 1 RBCs) The important contribution of this work is to determine the full modulus distribution of the blood samples and this is critical in comparing with different pathological states, since we observe a distinct difference in shear modulus distribution of different healthy individuals. The estimated shear modulus mean across all measurements of the fresh RBCs of healthy donors (13.2 µN m^{-1}) is consistent with published values of optical tweezers (11-20 µN m^{-1}),[24,32] micropipette aspiration (9-10 µN m^{-1}),[55,59] and membrane fluctuation (7.4 µN m^{-1}).[25] Our estimated shear modulus standard deviation is larger than these methods (Fig. S12).
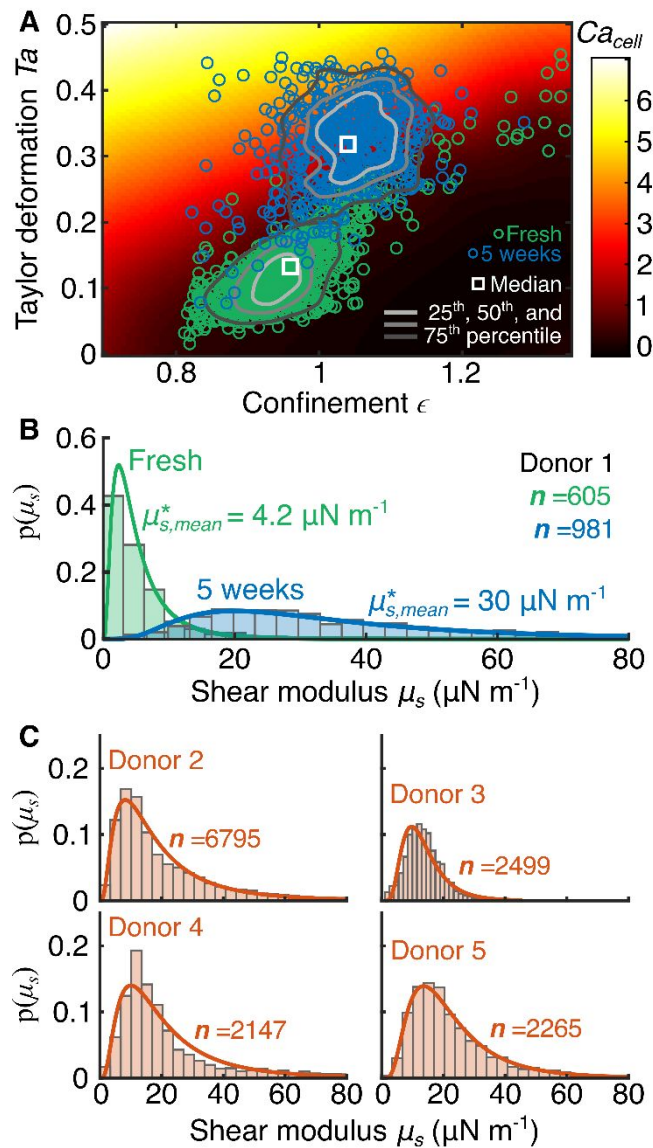
1

Fig. 5. (A) Experimentally measured Taylor deformation Ta versus confinement ϵ data for Donor 1 RBCs that were freshly withdrawn (green, open circles) and 5-weeks stored in a 4°C fridge (blue, open circles). The white square and the solid lines respectively denote the median Ta and ϵ and the 25th, 75th, and 75th percentiles of each group. The scattered data is overlaid on the computationally generated Ta versus ϵ surface which results in a single capillary number of the cell Ca_{cell}. (B) Shear modulus distributions corresponding to the same data set (fresh in green and 5-weeks stored in blue). The value $\mu_{s,mean}^*$ denotes the geometric mean shear modulus of each group. (C) Shear modulus distributions for freshly withdrawn RBCs from Donors 2-5. n is the number of cells analyzed in each group.

3 Concluding remarks

We have designed a high-throughput microfluidic platform for measuring the shear modulus distribution of an individual's RBCs. This was accomplished by fabricating microchannels with square cross-sections (7 by 7 μm) such that, under specified conditions, RBCs assume a steady-state parachute shape 300 μm downstream of the channel entrance. We then determined the Taylor deformation parameter Ta using a custom, robust, and automated single-cell tracking and shape quantification algorithm. Our simulations indicated that Ta is both sensitive to RBC shear modulus and smoothly and uniquely approaches a steady-state value independent of the initial condition. These are superior features compared to the other deformation parameters used in the literature, such as circularity or elongation index.

We further utilized our 3D numerical model to construct a three-dimensional surface that is used to find the shear modulus of individual cells based on the experimentally measured values of Ta, confinement ϵ, and cell velocity U_{cell}. The corresponding figures of merit that we developed are based on dimensionless numbers and therefore are generically applicable to measure the shear moduli of RBCs under different geometrical or operational conditions. We note, however, that our model does not accurately describe the shape-governing properties of abnormal cells such as sickle RBCs or schistocytes. Our current system is limited to measurement of the shear moduli for discoid-shaped RBCs which assume a parachute shape under flow and confinement.

Finally, we conducted experiments with blood samples from several healthy individuals and quantified the impact of sample storage in a 4°C fridge for 5 weeks. Our results indicate very good agreement with the range of shear modulus that is obtained using optical tweezers, micropipette aspiration, and membrane fluctuation. Consistent with the literature, we found that the average modulus of the stored cells is up to three times larger than fresh samples and the distribution of modulus significantly broadens. The distribution of the shear modulus, as was introduced in this paper, may be essential to determine the healthy and diseased status of an individual's RBCs. We have determined this distribution with much higher precision than has been accomplished previously, and this is a direct result of our ability to image with high temporal and spatial resolution each of thousands of cells multiple times in a short time period. We believe that such measurements will be critical to disease detection and evaluation of pharmaceutical treatments.

4 Methods

4.1 Immersed finite-element method

An immersed finite-element method (a variant of the IB technique) was used[49] to determine the shape evolution in three different geometries which constitute our microfluidic channels; a non-periodic entrance region, a periodic straight channel with square cross-section, and a non-periodic exit region (cf. Fig. S1). A 3D biconcave structure was used for RBCs with highly refined triangular mesh (10,242 mesh nodes per cell). The membrane elastic properties, such as shear and bending moduli as well as physiological cytoplasmic viscosity were included in our RBC model.

In addition, our simulation algorithm is massively parallelized and uses a distributed message passing interface (MPI) for both the fluid flow solver as well as stress calculation in the solid domain.[49] This feature substantially reduces the execution time of our simulation described in Fig. S1, making it tractable despite high degrees of refinement for both fluid and solid domains.

4.2 Nondimensional parameters

A total of six dimensionless parameters describe the physical system (further described in SI, Section S.1). The first three are the Reynolds number ($Re = \rho U H / \eta$), the cytoplasmic viscosity ratio ($\lambda = \eta_{cell}/\eta$), and the capillary number ($Ca = \eta U / \mu_s$), all of which appear in the fluid and solid conservation of momentum equations. Two additional ratios appear in the membrane constitutive equations: μ_d/μ_s and $\kappa_b = \dfrac{k_b}{H\mu_s}$. The dimensional parameters include: ρ, the density, U, the bulk velocity inside the constriction, H, the channel height (or width), η and η_{cell}, the viscosity of the medium fluid and the cytoplasm, respectively, and finally μ_s and μ_d are the shear and dilatational moduli. The last dimensionless parameter is a geometric parameter, termed the "confinement" ϵ (cf. Section 2.1) which is the ratio of the cell projected effective diameter to the channel dimension. With these assumptions, the only dimensionless parameters that may significantly vary from cell to cell (and thus govern the physics of our problem) are Ca and ϵ.

The Reynolds number is set to 10^{-1} for all of the simulations in this study. We used the well-known Skalak model[60] for modelling the RBC membrane and assume, as usual, that these systems are largely surface incompressible. Note that the shear modulus in the Skalak model is constant and for all shear strains considered in the model calculations in this work, this is an accurate approximation. However, at very large shear strain, for instance in splenic filtration process[4] or at very high confinement levels, the shear strain can be much greater than unity and the shear modulus can significantly change.[6] In such cases, other suitable models, such as the hyperplastic effective material model [24] can be used. Thus, we set the dimensionless ratio: $\dfrac{\mu_d}{\mu_s}$ $= 100$. The bending parameter, κ_b, is generally found to be much smaller than unity[61] and inconsequential—we set it to 0.0033 for all of the simulations.

The problem domain is either the entrance region of the microchannel, or a straight channel with periodic boundary condition (see Fig. 1A and SI, Fig. S1). For the former, the fluid

flow is imposed at the inlet, such that, we achieve the characteristic velocity $\bar{u}$ at the constriction. For the periodic domain, a pressure drop is imposed which results in the unperturbed average velocity U at the constriction.

4.3 Comparison of shape factors

The choice of the shape factor used to quantify cell deformation is critical to ensure sensitivity to the key variables, i.e. the capillary number Ca and the confinement ϵ. First, we used simulations to show that the steady state cell Taylor deformation Ta is more sensitive to shear modulus than are the circularity (also called "form factor")[62] C, circular harmonics coefficients c_i, and the deformation ratio DR. Large differences in Ca (factor of 8) resulted in small difference in C (factor of 1.13), as shown in Fig. S2. The circular harmonics coefficients (Fig. S3) showed a slightly better result (8-fold differences in Ca resulted in 2-fold differences in coefficient values). DR was shown to be largely insensitive to Ca (Fig. S4 and Table 1). Moreover, our simulations and experiments indicate that many of the cells evolve to a skewed (or oriented) configuration which can potentially affect other deformation indices, but not Ta (Figs. 2 and S5).

Finally, we investigated the contribution of image noise to the determination of the shape factors Ta, C,[63] eccentricity ε,[64] compactness C_{comp},[65] and DR (cf. SI, Section S.8).[38,63] The steady state shape factors for individual cell trajectories were computed (left of Fig. S14) and variations in these values for a single cell were attributed to image noise. That is, detection algorithms which track and quantify the contour length of the cell boundaries are sensitive to this image noise. These perturbations cause the detection algorithm to produce different cell boundary contour lengths from frame to frame. We observed and quantified (right of Fig. S14) that shape factors determined by zero order moments of the cell image (e.g. C and DR) are more sensitive to image noise than are shape factors determined by second order moments (e.g. Ta, ε, and C_{comp}).

5 Author contributions

E.S.G.S., and J.G.S. led conceptualization. A.S. and E.S.G.S. led the computational approach. A.S. led the computational implementation. D.A.H., D.I.O., and J.G.S. led conceptualization of the experimental setup. D.A.H. and D.I.O. led implementation of the experimental setup, data curation, and image analysis software. P.V.E., I.O., D.A.H., and D.I.O. performed the experiments. A.S. helped in running experiments and image analysis. P.V.E supported the data visualization, computer code development, and experimental investigation. D.A.H., D.I.O., and A.S. led the writing of the manuscript.
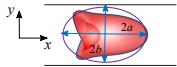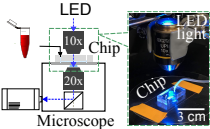
6 Acknowledgements

7 References

1   I. V Pivkin, Z. Peng, G. E. Karniadakis, P. A. Buffet, M. Dao and S. Suresh, *Proc. Natl. Acad. Sci.*, 2016, **113**, 7804–7809.

2   R. Huisjes, A. Bogdanova, W. W. van Solinge, R. M. Schiffelers, L. Kaestner and R. van Wijk, *Front. Physiol.*, , DOI:10.3389/fphys.2018.00656.

3   P. Gambhire, S. Atwell, C. Iss, F. Bedu, I. Ozerov, C. Badens, E. Helfer, A. Viallat and A. Charrier, *Small*, 2017, **13**, 1700967.

4   H. Lu and Z. Peng, *Phys. Fluids*, 2019, **31**, 31902.

5   S. Salehyar and Q. Zhu, *Soft Matter*, 2016, **12**, 3156–3164.

6   Y. Kim, K. Kim and Y. Park, .

7   J. Kim, H. Lee and S. Shin, *J. Cell. Biotechnol.*, 2015, **1**, 63–79.

8   S. Suresh, J. Spatz, J. P. Mills, A. Micoulet, M. Dao, C. T. Lim, M. Beil and T. Seufferlein, *Acta Biomater.*, 2005, **1**, 15–30.

9   T. Wu and J. J. Feng, *Biomicrofluidics*, 2013, **7**, 44115.

10   T. Ye, N. Phan-Thien, B. C. Khoo and C. T. Lim, *Biophys. J.*, 2013, **105**, 1103–1109.

11   L. Diederich, T. Suvorava, R. Sansone, T. C. S. Keller IV, F. Barbarino, T. R. Sutton, C. M. Kramer, W. Lückstädt, B. E. Isakson, H. Gohlke and others, *Front. Physiol.*

12   A. S. Smith, R. B. Nowak, S. Zhou, M. Giannetto, D. S. Gokhin, J. Papoin, I. C. Ghiran, L. Blanc, J. Wan and V. M. Fowler, *PNAS*, 2018, **115**, E4377–E4385.

13   K. Tsukada, E. Sekizuka, C. Oshio and H. Minamitani, *Microvasc. Res.*, 2001, **61**, 231–239.

14   A. G. Moutzouri, G. A. Athanassiou, D. Dimitropoulou, A. T. Skoutelis and C. A. Gogos, *J. Infect.*, 2008, **57**, 147–151.

15   O. K. Baskurt, D. Gelmont and H. J. Meiselman, *Am. J. Respir. Crit. Care Med.*, 1998, **157**, 421–427.

16   A. G. Moutzouri, A. T. Skoutelis, C. A. Gogos, Y. F. Missirlis and G. M. Athanassiou, *Clin. Hemorheol. Microcirc.*, 2007, **36**, 291–299.

17   N. F. Zeng, J. E. Mancuso, A. M. Zivkovic, J. T. Smilowitz and W. D. Ristenpart, *PLoS*

One, 2016, **11**, e0156070.

18   S. Zhou, M. Giannetto, J. DeCourcey, H. Kang, N. Kang, Y. Li, S. Zheng, H. Zhao, W. R. Simmons, H. S. Wei, D. M. Bodine, P. S. Low, M. Nedergaard and J. Wan, *Sci. Adv.*, 2019, **5**, eaaw4466.

19   H. S. Wei, H. Kang, I.-Y. D. Rasheed, S. Zhou, N. Lou, A. Gershteyn, E. D. McConnell, Y. Wang, K. E. Richardson, A. F. Palmer, C. Xu, J. Wan and M. Nedergaard, *Neuron*, 2016, **91**, 851–862.

20   M. Dao, J. Li and S. Suresh, *Mater. Sci. Eng. C*, 2006, **26**, 1232–1244.

21   C. Pozrikidis, *Phys. Fluids*, 2005, **17**, 31503.

22   R. M. Hochmuth, P. R. Worthy and E. A. Evans, *Biophys. J.*, 1979, **26**, 101–114.

23   E. A. Evans and R. M. Hochmuth, *Biophys. J.*, 1976, **16**, 1–11.

24   M. Dao, C. T. Lim and S. Suresh, *J. Mech. Phys. Solids*, 2003, **51**, 2259–2280.

25   Y. Park, C. A. Best, K. Badizadegan, R. R. Dasari, M. S. Feld, T. Kuriabova, M. L. Henle, A. J. Levine and G. Popescu, *Proc. Natl. Acad. Sci.*, 2010, **107**, 6731–6736.

26   G. Tomaiuolo, *Biomicrofluidics*, 2014, **8**, 51501.

27   Y. Kim, K. Kim and Y. Park, in *Blood cell-An overview of studies in hematology*, InTech, 2012.

28   D. A. Fedosov, B. Caswell, S. Suresh and G. E. Karniadakis, *Proc. Natl. Acad. Sci.*, 2011, **108**, 35–39.

29   E. Evans, N. Mohandas and A. Leung, *J. Clin. Invest.*, 1984, **73**, 477–488.

30   Q. Guo, S. Park and H. Ma, *Lab Chip*, 2012, **12**, 2687–2695.

31   R. M. Hochmuth, *J. Biomech.*, 2000, **33**, 15–22.

32   H. Song, Y. Liu, B. Zhang, K. Tian, P. Zhu, H. Lu and Q. Tang, *Biomed. Opt. Express*, 2017, **8**, 384–394.

33   P. M. Davidson, G. R. Fedorchak, S. Mondésert-Deveraux, E. S. Bell, P. Isermann, D. Aubry, R. Allena and J. Lammerding, *Lab Chip*, 2019, **19**, 3652–3663.

34   X. Liu, Z. Tang, Z. Zeng, X. Chen, W. Yao, Z. Yan, Y. Shi, H. Shan, D. Sun, D. He and others, *Math. Biosci.*, 2007, **209**, 190–204.

35   N. Yeow, R. F. Tabor and G. Garnier, *Adv. Colloid Interface Sci.*

36   I. Dulińska, M. Targosz, W. Strojny, M. Lekka, P. Czuba, W. Balwierz and M. Szymoński, *J. Biochem. Biophys. Methods*, 2006, **66**, 1–11.

37   S. E. Barns, Queensland University of Technology, 2018.

38   J. C. A. Cluitmans, V. Chokkalingam, A. M. Janssen, R. Brock, W. T. S. Huck and G. J. Bosman, *Biomed Res. Int.*

39   A. M. Forsyth, J. Wan, W. D. Ristenpart and H. A. Stone, *Microvasc. Res.*, 2010, **80**, 37–43.

40   O. Otto, P. Rosendahl, A. Mietke, S. Golfier, C. Herold, D. Klaue, S. Girardo, S. Pagliara, A. Ekpenyong, A. Jacobi, M. Wobus, N. Töpfner, U. F. Keyser, J. Mansfeld, E. Fischer-

Friedrich and J. Guck, *Nat. Methods*, 2015, **12**, 199–202.

41 B. Fregin, F. Czerwinski, D. Biedenweg, S. Girardo, S. Gross, K. Aurich and O. Otto, *Nat. Commun.*, , DOI:10.1038/s41467-019-08370-3.

42 F. Reichel, J. Mauer, A. A. Nawaz, G. Gompper, J. Guck and D. Fedosov, *Biophys. J.*, 2019, **117**, 14–24.

43 K. R. M., S. Bhattacharya, S. DasGupta and S. Chakraborty, *Lab Chip*, 2018, **18**, 3939–3948.

44 M. Mokbel, D. Mokbel, A. Mietke, N. Träber, S. Girardo, O. Otto, J. Guck and S. Aland, *ACS Biomater. Sci. Eng.*, 2017, **3**, 2962–2973.

45 Z. Xu, Y. Zheng, X. Wang, N. Shehata, C. Wang and Y. Sun, *Microsystems Nanoeng.*

46 N. Mehendale, D. Mitra and D. Paul, *bioRxiv*, 2019, 644161.

47 C. S. Peskin, *J. Comput. Phys.*, 1977, **25**, 220–252.

48 L. T. Zhang and M. Gay, *J. Fluids Struct.*, 2007, **23**, 839–857.

49 A. Saadat, C. J. Guido, G. Iaccarino and E. S. G. Shaqfeh, *Phys. Rev. E*, , DOI:10.1103/PhysRevE.98.063316.

50 A. Saadat, C. J. Guido and E. S. G. Shaqfeh, *bioRxiv*, 2019, 572933.

51 A. Raj, M. Dixit, M. Doble and A. K. Sen, *Lab Chip*, 2017, **17**, 3704–3716.

52 K. Sinha and M. D. Graham, *Phys. Rev. E*, 2015, **92**, 42710.

53 A. Z. K. Yazdani, Rutgers, 2012.

54 T. W. Secomb, *Annu. Rev. Fluid Mech.*, 2017, **49**, 443–461.

55 Y. C. Fung, *Biomechanics: Circulation*, Springer, 1997.

56 J. G. Santiago, S. T. Wereley, C. D. Meinhart, D. J. Beebe and R. J. Adrian, *Exp. Fluids*, 1998, **25**, 316–319.

57 E. Limpert and W. A. Stahel, *Significance*, 2017, **14**, 8–9.

58 R. P. Sorrentino, *Fly*, 2010, **4**, 327–332.

59 E. A. Evans, R. Waugh and L. Melnik, *Biophys. J.*, 1976, **16**, 585–595.

60 R. Skalak, A. Tozeren, R. P. Zarda and S. Chien, *Biophys. J.*, 1973, **13**, 245–264.

61 E. A. Evans, *Biophys. J.*, 1983, **43**, 27–30.

62 L. L. Wheeless, R. D. Robinson, O. P. Lapets, C. Cox, A. Rubio, M. Weintraub and L. J. Benjamin, *Cytometry*, 1994, **17**, 159–166.

63 M. Urbanska, H. E. Muñoz, J. Shaw Bagnall, O. Otto, S. R. Manalis, D. Di Carlo and J. Guck, *Nat. Methods*, 2020, 1–7.

64 C. Fatichah, D. Purwitasari, V. Hariadi and F. Effendy, *Int. J. Smart Sens. Intell. Syst.*, 2014, **7**, 1271–1286.

65 P. Ruusuvuori, A. Lehmussola, J. Selinummi, T. Rajala, H. Huttunen and O. Yli-Harja, *Eur. Signal Process. Conf.*

2